Article

Parameter Tuning Method for a Lattice Compensated Wireless Power Transfer System

Ebrahim Nasr Esfahani * and Indranil Bhattacharya *

Department of Electrical and Computer Engineering, Tennessee Technological University, Cookeville, TN 38505, USA
* Correspondence: enasresfa42@tntech.edu (E.N.E.); ibhattacharya@tntech.edu (I.B.)

Abstract: This study presents a new charging system with lattice compensation for wireless power transfer (WPT) applications. A mathematical model is developed for the proposed system to accurately estimate power transfer capabilities. Furthermore, a linear programming algorithm is used to find the proper values for lattice compensation, which helps achieve high efficiency over a wide range of loads and zero voltage switching (ZVS) for the proposed system. The approach is validated through analysis, modeling, and simulation of a 3-kilowatt WPT system. Additionally, a 200-watt prototype with a 100 mm air gap was built and tested, showing an efficiency of 86.3% during charging. This method eliminates the need for an auxiliary DC–DC converter, ensuring efficient charging across various load conditions. The prototype's performance closely matches the simulation results, indicating its potential for scaling up to electric vehicle (EV) battery charging applications.

Keywords: wireless power transfer; compensation; resonant network; winding-cross-coupled inductor; multi-objective optimization; two-part model; lattice network

1. Introduction

Electric vehicles (EVs) have received widespread attention due to their environmentally friendly nature, and the development of charging infrastructures is a critical factor in ensuring a smooth transition to EVs [1]. Wireless power transfer (WPT) is a pivotal technology for EVs, as it eliminates the need for driver intervention during the charging process [2]. This technology is also expected to play a significant role in advancing self-driving car technology [3]. WPT can be categorized into two primary types based on their operating principles: inductive power transfer (IPT), which utilizes electromagnetic induction, and capacitive power transfer (CPT), which employs high-frequency electric fields. Among these, IPT is the predominant method used in the EV industry for wirelessly transferring power at the kilowatt level, with most applications relying on magnetic fields for power transfer. Consequently, in this paper, the term WPT specifically refers to IPT [4]. Figure 1 illustrates the components of a typical inductive WPT system. This system comprises a high-frequency inverter, compensation networks, primary and secondary magnetically coupled coils, a rectifier, and a load. The large air gap between the coils results in relatively low magnetic coupling. Magnetic ferrites are often employed to enhance this coupling. Compensation networks, which include one or more inductors and capacitors, are required on both the primary and secondary sides to resonate with the coils. These networks are crucial for enhancing power transfer capability, canceling reactive power, achieving zero-phase angle (ZPA), and improving system efficiency. Although various compensation networks have been proposed in the literature, they often suffer from low power transfer efficiency. Detailed analyses and comparisons of these networks can be found in [5,6]. Large air gaps between the transmitter and receiver, as well as misalignment, are two major barriers that can hinder the widespread adoption of WPT systems for EV applications. Additionally, load-dependent charging characteristics in existing WPT systems negatively impact battery

charging efficiency. Each of these obstacles reduces transfer efficiency due to variations in system parameters. Consequently, achieving various objectives with either a simple pad or basic compensation is challenging. Research efforts aimed at addressing these issues in WPT systems can be categorized into two main approaches. The first approach focuses on mitigating the impact on power transfer by redesigning magnetic couplers or coil geometries. Several geometries and pad structures have been discussed in the literature, including double-D (DD) and double-D quadrature (DDQ), bipolar (BP) pads, and reconfigurable structures such as the tripolar design [6–8]. Alternatively, many researchers have proposed evolutionary algorithms (EAs) to find the optimal solution for pad design [9,10]. However, since the finite element method (FEM) is involved in the optimization process, these techniques often cannot complete their tasks in a reasonable time frame [11]. The second approach focuses on designing novel compensation networks or optimizing classic compensation parameters to improve overall system efficiency. Various resonant network designs have been proposed to achieve the desired output power and high efficiency under conditions of misalignment and varying loads. As illustrated in Figure 2, these methods can be categorized into three primary groups: basic resonant networks, hybrid topologies, and variable resonant networks.
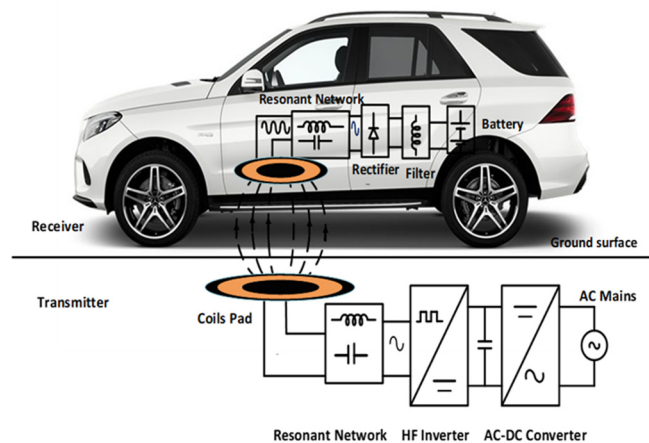
Figure 1. The concept of wireless charging and components of WPT system.
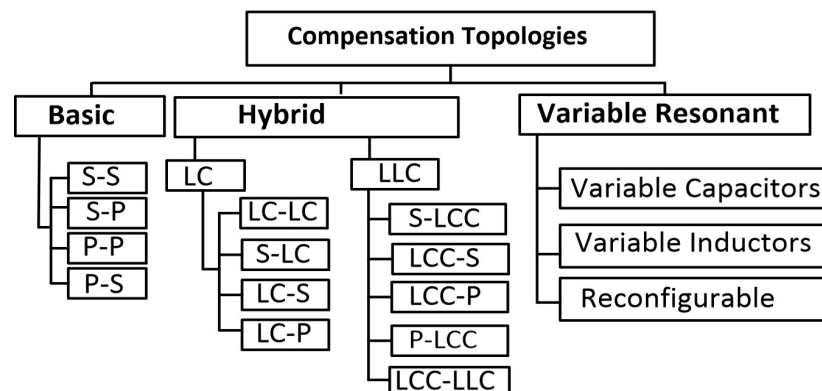
Figure 2. General classification of resonant network topologies for WPT systems.

The first "S" or "P" refers to the capacitor connected in series or parallel to the primary coil, while the second "S" or "P" represents the capacitor in series or parallel with the secondary coil. The S-S topology is selected in many applications for its simplicity, low component count, and high efficiency at the nominal operating point. However, this topology is highly sensitive to the misalignment of the magnetic couplers. Other simple topologies, such as those with a parallel resonant network on the secondary side, suffer from excessive output voltage under light-load conditions. Moreover, the P-P topology suffers

from a low input power factor, as seen by the inverter. PS topologies require a current input source, and SP topologies are incapable of blocking the DC component [12]. Hybrid topologies combine inductor or capacitor circuits with resonance components positioned on either the transmitter or the receiver. Variable inductors and capacitors can also be used to regulate the output voltage [13]. Nevertheless, detectors and controllers are necessary to enable reconfiguration, which complicates the control strategy. In [14], the addition of a saturable inductor to tune the resonant network is proposed. The disadvantage of this solution is that the magnetic core generates significant heat due to saturation.

Various higher-order compensation topologies have been explored to increase transfer efficiency. The inductor–capacitor–capacitor (LCC) topology is widely studied and can be used on either one or both sides, where each side consists of an external inductor (L), a series capacitor (C), and a parallel capacitor. A reconfigurable topology combining the characteristics of LCC-S and S-LCC into one resonant tank for output voltage regulation under load variations is proposed in [15]. However, the need for an extra coil pad increases both the weight and cost of the coils. In [16], the inductor of the LCC resonant network is integrated with the magnetic couplers. The main challenge of integrated compensation WPT systems is the design complexity caused by the interaction between the main coils and the compensation coils.

Load variations during charging make it challenging to maintain high efficiency and achieve zero voltage switching (ZVS). To address this, several methods have been proposed, including the use of active rectifiers such as semi-active rectifiers, full-bridge active rectifiers, and additional DC–DC converters on the primary, secondary, or both sides. These converters regulate the output voltage and provide constant current (CC) and constant voltage (CV) modes for charging EV batteries. In [17], a study reported an efficiency of 90.1% at 200 W and 294 kHz, proposing a WPT system using a buck converter on the primary side. However, this system is highly sensitive to circuit changes. In [18], Chunwei et al. proposed replacing the full-bridge circuit on the secondary side with a novel cascaded buck active rectifier. This approach avoids the need for a connection between the two sides and can achieve high efficiency under impedance mismatch conditions. However, it complicates the control system and requires output detection circuits to identify whether the system output is CC or CV. In [19], a variable frequency modulation approach is proposed for a WPT system to achieve a fixed output voltage. However, ZVS is only achieved at certain charging points. Another drawback of WPT charger systems with LLC compensation is their inherent limitation in managing inrush current during short circuits.

The X-shape topology, initially proposed with a single-sided lattice network by Alireza et al. [20], has all the advantages of LLC topologies. However, compensation network optimization has not been discussed. Although a few studies have been proposed for other resonant networks, further research is needed to optimize these systems. Fabio et al. in [21] introduced parameter tuning of the LLC/S compensation topology through a genetic algorithm and Monte Carlo optimization process. Despite achieving a finely tuned system, the optimization procedure remains both time-consuming and complex. Additionally, the approach is effective only under specific conditions, such as fixed coupling factors or load. Any deviation from these conditions results in the optimization failing to converge and obtain trapped in local optima.

In this paper, to address the aforementioned problems in traditional LLC topologies, a new lattice network topology is presented. The architecture of the proposed topology is an X-shaped circuit derived by employing winding-cross-coupled impedance. One of the distinct advantages of the proposed method is its capability for open- and short-circuit immunity in a WPT system, a capability previously validated and documented in [22]. The proposed WPT system can perform buck-boost functions, eliminating the need for additional DC–DC converters, unlike traditional LLC topologies. The proposed topology structure of the lattice network is introduced, and its working principle is analyzed. Then, the inherent relationship between the output power and mutual inductance is derived. In addition, to clearly show the variation of the design parameters, a single parameter

variation is studied for each component in the lattice network. This paper also proposes a new approach that is based on an integer linear programming algorithm to determine the most desirable value for adjusting the parameters of a resonant network. Finally, the experimental results verify the effectiveness of the proposed method. The major contributions of this article are summarized in the following:

- A novel WPT system with a lattice resonant network is proposed. Compared with the traditional method, the additional DC—DC converter can be reduced, thereby saving cost and weight.
- A T model for double-side lattice in the suggested system is developed, and its working mode and output characteristics are analyzed in detail.
- A new optimization technique was developed to design the lattice resonant network. To achieve output voltage regulation and ZVS during the charging process, ultimately extending battery life.

The remaining part of this paper is organized as follows: Section 2 introduces the mathematical formulation of the WPT system with a lattice-based network. In Section 3, the sensitivity analysis is detailed, examining how variations in parameters such as passive components, load, and resonant frequency affect the output voltage and transfer efficiency of the proposed system. Section 4 defines the objective function of the system and discusses the optimization technique using linear programming. Section 5 presents the experimental prototype, describing the construction and testing process to validate the feasibility and accuracy of the theoretical analysis and simulation results. Finally, Section 6 summarizes the conclusions drawn from the study and provides an outlook on future research directions and potential improvements.

2. Proposed Topology and Analysis

This section provides a comprehensive overview of the theoretical foundations and key mathematical equations pertinent to the configuration and modeling of lattice circuits.

2.1. Lattice Circuit Configuration and Modeling

The lattice network structure has been utilized in a wide range of applications over the past few decades due to its effectiveness in rejecting electromagnetic [23].

Figure 3 presents a symmetrical lattice shape structure. The arms with impedances Z_1 are called series arms, while the arms with impedances Z_2 are called diagonal arms. In the WPT system, arms consider $Z_1 = L_z\omega$ and $Z_2 = 1/C_z\omega$. The lattice could be analyzed as a two-port model, which is described by four variables: V_1, I_1, V_2, and I_2. Two of the variables are used as excitation variables, and the other two are used as response variables. Based on the different combinations, four kinds of two-port parameters could be derived, referred to as Y, Z, G, and H-parameters. The lattice network is modeled using G-parameters, as shown in Figure 3b. The terminal voltages and currents can be described as [24]:

$$\begin{bmatrix} I_1 \\ V_2 \end{bmatrix} = \begin{bmatrix} g_{11} & g_{12} \\ g_{21} & g_{22} \end{bmatrix} \begin{bmatrix} V_1 \\ I_2 \end{bmatrix} \tag{1}$$

The G-parameters for lattice can be determined by using Figure 3b as a reference.

$$g_{11} = \frac{2}{j\omega L_Z + \frac{1}{j\omega C_z}} = \frac{2j\omega C_z}{1 - \omega^2 L_z C_z} \tag{2}$$

$$g_{12} = g_{21} = \frac{-j\omega L_Z + \frac{1}{j\omega C_z}}{j\omega L_Z + \frac{1}{j\omega C_z}} = \frac{1 + \omega^2 L_z C_z}{1 - \omega^2 L_z C_z} \tag{3}$$

$$g_{22} = \frac{\frac{2j\omega L_z}{j\omega C_z}}{j\omega L_Z + \frac{1}{j\omega C_z}} = \frac{2j\omega L_z}{1 - \omega^2 L_z C_z} \tag{4}$$
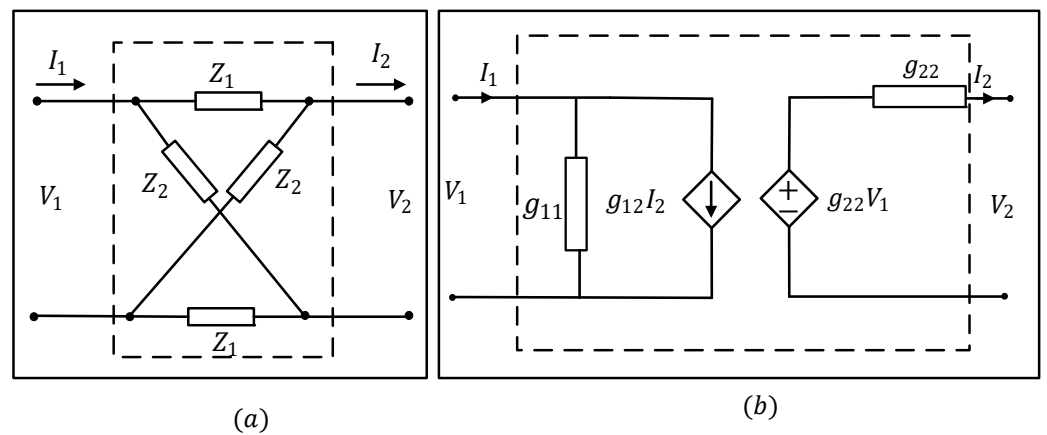
Figure 3. (**a**) Symmetrical lattice network; (**b**) the G-parameter description of the lattice network.

For simplicity of analysis, the lattice network's resonant frequency is written as:

$$\begin{bmatrix} I_1 \\ V_2 \end{bmatrix} = \frac{1}{1 - \omega^2 L_z C_z} \begin{bmatrix} j2\omega C_z & 1 + \omega^2 L_z C_z \\ 1 + \omega^2 L_z C_z & j2\omega C_z \end{bmatrix} \begin{bmatrix} V_1 \\ I_2 \end{bmatrix} \tag{5}$$

Additionally, the normalized operating frequency α in relation to the resonant frequency of the network can be written as:

$$\alpha = \frac{\omega}{\omega_z} \tag{6}$$

If (5) is replaced with (6) then

$$\begin{bmatrix} I_1 \\ V_2 \end{bmatrix} = \frac{1}{1 - \omega^2 L_z C_z} \begin{bmatrix} \frac{j2\omega L_z}{1-\alpha^2} & \frac{1+\alpha^2}{1-\alpha^2} \\ \frac{1+\alpha^2}{1-\alpha^2} & \frac{j2\omega L_z}{1-\alpha^2} \end{bmatrix} \begin{bmatrix} V_1 \\ I_2 \end{bmatrix} \tag{7}$$

The lattice network's equivalent output inductance $L_{eq} = 2L_z/(1 - \alpha^2)$ and $C_{eq} = 2C_z/(1 - \alpha^2)$ provides the compensatory functionality like external and capacitor and inductor in LLC topology to compensate for the large reactive impedance. With the appropriate range of values for the parameter α, it is possible to transform the G-parameter description into an equivalent circuit model, as depicted in Figure 4a. The turns ratio (N_z), as well as the normalized values of L_{eq}/L_z and C_{eq}/L_z, all plotted against the normalized frequency α, are depicted in Figure 4b.
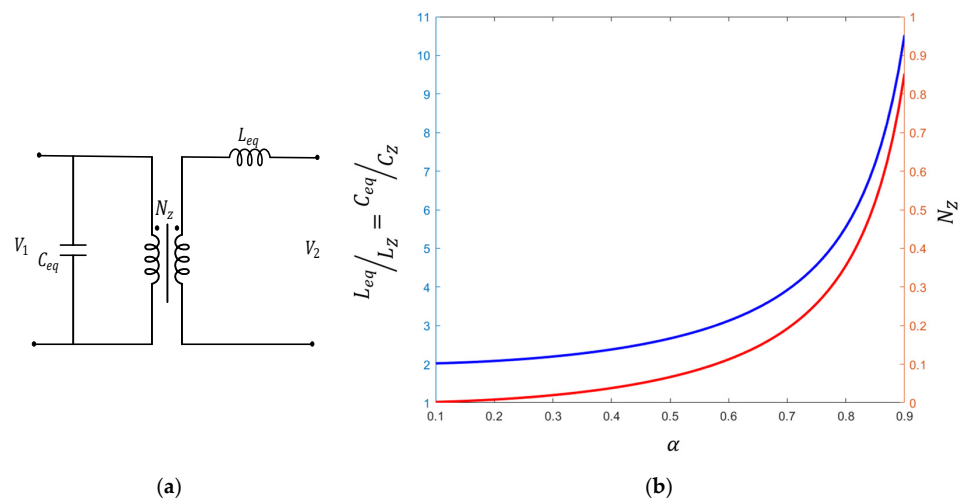
Figure 4. (**a**) Equivalent circuit model of the lattice network: (**b**) N_Z and $L_{eq}/L_z (= C_{eq}/L_c)$ vs. α.

When the operating frequency closely matches the resonant frequency of the lattice network, it has the potential to increase voltage since the ideal transformer ratio $N_z = 1 + \alpha^2 / (1 - \alpha^2)$ is always greater than one when α is less than one. Thus, it can perform boost functions, as compared to the LLC. As a result, adjusting the normalized frequency at various points in the lattice network enables the modification of its characteristics. Thus, it can perform buck–boost functions, as compared to the traditional LLC. Consequently, it helps to reduce the need for additional DC–DC converters for voltage regulation. Thus, at this point, α shows a low sensitivity to variations in load resistance, indicating that there may not be significant power fluctuations when there is a drift in load resistance.

2.2. Circuit Models of the Proposed Lattice Compensated WPT System

The concept of lattice compensation is introduced in this part. Figure 5 shows the structure of the proposed WPT system with the lattice compensation network. It includes a high-frequency inverter, a series resonant tank, a lattice compensation network, an inductive coupling interface consisting of two pairs of coupling pads, and a full-bridge rectifier followed by a capacitive filter and a battery. Parasitic resistances are neglected for simplification. The WPT system is fed by a square-wave ac voltage V_{AB} generated by the full-bridge inverter. The lattice circuits are utilized to create resonance for the primary and secondary coils.
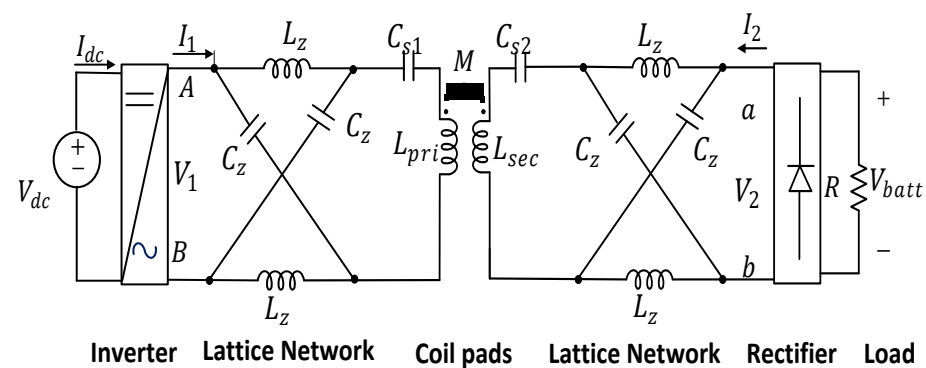
Figure 5. The proposed topology with double-sided lattice compensation network.

A full-bridge rectifier converts the ac voltage V_{ab} to DC voltage V_{batt} to feed the load. The high-order resonant network absorbs the higher harmonics of the inverter voltage. Therefore, for the simplicity of the analysis and design of the resonant network, a fundamental harmonic analysis (FHA) is commonly used. According to the FHA, the voltage-source rectifier and the load R can be equivalent to a resistance R_{leq}, defined as follows [25]:

$$R_{leq} = \frac{8}{\pi^2 R} \tag{8}$$

The operating frequency of the system is at $f_o = 85$ kHz, as specified by the SAE J2954 standard [25].

2.3. Basic Analysis of the Lattice Circuit

The mathematical expression of the lattice-compensated WPT converter has not been appropriately solved, which leads to difficulties in the analysis of the WPT system. Thus, the lattice-compensated WPT converter should be designed with a zero phase angle (ZPA) frequency operation. It is necessary to calculate the input impedance of the system. The WPT converter can be simplified as an equivalent two-port network with the transmission matrix T. It consists of two lattice, two capacitor, and two coil pads.

$$\begin{bmatrix} V_{in} \\ I_{in} \end{bmatrix} = T \begin{bmatrix} V_o \\ I_o \end{bmatrix} \tag{9}$$

As shown in Figure 6, by using the T model of the coupling coils (T_m), the T model of the series capacitor (T_c) and the model of the lattice network Z_{lts}, the equivalent circuit of the proposed multichannel WPT system can be obtained.
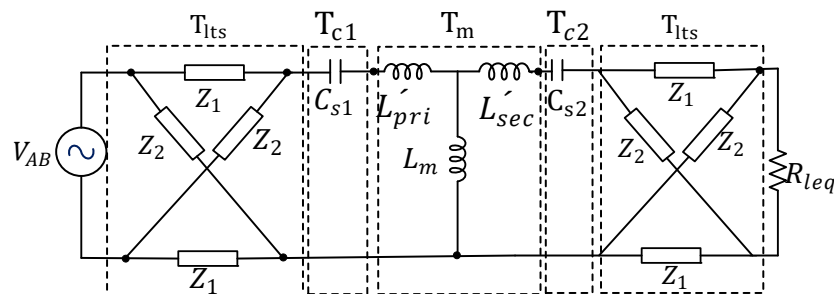
Figure 6. Schematic of the cascaded T model of the proposed double-sided lattice network-impedance as a two-port network.

T_M is used to illustrate the coupling coils. (L'_{pri}) and (L'_{sec}) are the leakage inductances of the transmitter and receiver coils, which can be expressed as follows:

$$L'_{pri} = L_{pri} - L_M \tag{10}$$

$$L'_{sec} = L_{sec} - L_M \tag{11}$$

by applying Kirchhoff's voltage law (KVL) around the loop in Figure 6, the lattice network shown can be described as a Z-parameters.

$$Z_{lts} = \begin{bmatrix} Z_1 + Z_2 & Z_2 - Z_2 \\ Z_1 - Z_2 & Z_1 + Z_2 \end{bmatrix} \tag{12}$$

By converting the Z-network to T-networks, a T-network of the circuit can be written as [24]:

$$T_{lts} = \begin{bmatrix} \dfrac{Z_{lts_{11}}}{Z_{lts_{21}}} & \dfrac{|Z_{lts_{21}}|}{Z_{lts_{21}}} \\ \dfrac{1}{Z_{lts_{21}}} & \dfrac{Z_{lts_{22}}}{Z_{lts_{11}}} \end{bmatrix} \tag{13}$$

The T-networks of series compensation capacitors are defined as follows:

$$T_{c1} = \begin{bmatrix} 1 & \dfrac{1}{j\omega C_{s1}} \\ 0 & 1 \end{bmatrix} \tag{14}$$

$$T_{c1} = \begin{bmatrix} 1 & \dfrac{1}{j\omega C_{s2}} \\ 0 & 1 \end{bmatrix} \tag{15}$$

The T-network of coil pads is defined as follow:

$$T_m = \begin{bmatrix} \dfrac{L_{pri}}{M} & j\omega\left(\dfrac{-jL_{pri}L_{sec}}{M} - M\right) \\ \dfrac{-j}{\omega M} & \dfrac{L_{sec}}{M} \end{bmatrix} \tag{16}$$

According to the principle of two-port networks, the transfer matrices of the five subnetworks are interconnected by

$$T = T_{lts} \times T_{c1} \times T_m \times T_{lts} \times T_{c2} \tag{17}$$

$$\begin{bmatrix} V_{in} \\ I_{in} \end{bmatrix} = \begin{bmatrix} A & C \\ B & D \end{bmatrix} \begin{bmatrix} V_o \\ I_o \end{bmatrix} \tag{18}$$

The input impedance of the proposed double-sided lattice network-impedance WPT system is calculated as Z_{in} [24]

$$Z_{in} = \frac{V_{in}}{I_{in}} = \frac{AZ_l + B}{CZ_l + D} \tag{19}$$

and the input phase angle between the input voltage and current of the resonant tank ϕ_{in} can be calculated by of the system is given as:

$$\phi_{in} = \frac{180}{\pi} \text{Arctan}\left(\frac{\text{Im}|Z_{in}|}{\text{Re}|Z_{in}|}\right) \tag{20}$$

where the operators "Im" and "Re" represent the real and imaginary components of the corresponding variable, respectively. The power transferred from the primary to the secondary is then simply the reflected resistance multiplied by the square of the primary current as given by

$$\text{P} = \frac{V_{in}^2}{\text{Re}(Z_{in})} \tag{21}$$

2.4. Double-Sided Lattice Network with Winding-Cross-Coupled Inductor

Figure 7 shows the lattice with a winding-cross-coupled combination of the passive inductor and capacitor components, where the primary side components L_{z1}, C_{z1}, C_{s1} and the secondary components L_{z2}, C_{z2}, C_{s2}. M_{z1} and M_{z2} are the mutual inductance between compensation inductors. WPT coils with primary and secondary inductances L_{pri}, L_{sec}, and a coupling coefficient of k, which demonstrates the magnetic coupling strength between self-inductance of L_{pri} and L_{sec} can be modeled as a coupled inductor with magnetizing inductance as

$$k = \frac{M}{\sqrt{L_{pri}\,L_{sec}}} \tag{22}$$
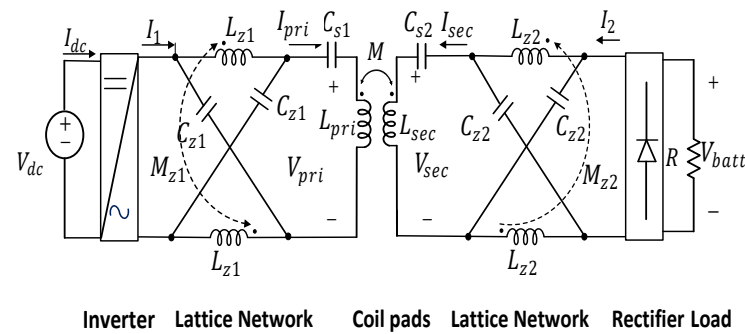
Figure 7. The proposed topology with a double-sided lattice compensation network by using a winding-cross-coupled inductor.

For WPT with winding-cross-coupled in high-order compensation networks, two factors must be considered when merging basic WPT and high-order compensations. First, the ZPA characteristic should not be impacted by using high-order compensations. Second, maintaining the load-independent output characteristics is still essential. Here, ω is the resonant frequency, which defines the switching frequency of the lattice-series resonant converter. The resonant relationships between the parameters are expressed as:

$$\omega = \frac{1}{\sqrt{\left(L_{z1} + M_{z1)}C_{z1}\right)}} = \frac{1}{\sqrt{L_{pri}\,C_{s1}}} \tag{23}$$

$$\omega = \frac{1}{\sqrt{\left(L_{z2} + M_{z2)}\right)C_{z2}}} = \frac{1}{\sqrt{L_{sec}\,C_{s2}}} \tag{24}$$

If the inductance and capacitance values of the lattice networks satisfy (23) and (24), C_{z1} will resonate with L_{z1} at the operating frequency ω. Similarly, C_{s2} also resonates with L_{sec} at the operating frequency ω. The lattice compensation with the winding-cross-coupled inductor is modeled and analyzed by using the Y parameters. In the Y-parameter model if V_1 and V_2 are inputs, then, I_1 and I_2 are linearly expressed with four parameters, Y_{11}, Y_{12}, Y_{21}, and Y_{22}, shown as follows.

$$\begin{bmatrix} I_1 \\ I_2 \end{bmatrix} = \begin{bmatrix} y_{11} & y_{12} \\ y_{21} & y_{22} \end{bmatrix} \begin{bmatrix} V_{z1} \\ V_{z2} \end{bmatrix} \tag{25}$$

$$y_{11} = \frac{1}{2}\left(\frac{1}{j\omega(L_{z1} + M_{z1})} + j\omega C_{z1}\right) \tag{26}$$

$$y_{12} = \frac{1}{2}\left(j\omega C_{z1} - \frac{1}{j\omega(L_{z1} + M_{z1})}\right) \tag{27}$$

$$y_{21} = -\frac{1}{2}\left(j\omega C_{z1} - \frac{1}{j\omega(L_{z1} + M_{z1})}\right) \tag{28}$$

$$y_{22} = -\frac{1}{2}\left(\frac{1}{j\omega(L_{z2} + M_{z2})} + j\omega C_{z1}\right) \tag{29}$$

In the resonant connection described in (23) and (24), the Y parameters will be reduced to:

$$Y = \begin{bmatrix} y_{11} & y_{12} \\ y_{21} & y_{22} \end{bmatrix} = \begin{bmatrix} 0 & -\frac{1}{j\omega(L_{z1}+M_{z1})} \\ \frac{1}{j\omega(L_{z2}+M_{z2})} & 0 \end{bmatrix} \tag{30}$$

The power transferred from the primary coil to the secondary coil at the resonant frequency can be written as:

$$P_{out} = \frac{k\,V_1 V_2}{\omega(L_{z1} + M_{z1})(L_{z2+} + M_{z2})} \tag{31}$$

3. Sensitivity Analysis

Generally, WPT is sensitive to parameter variations of the passive components, load, and resonant frequency. Even small-percent parameter variations can induce a large change in output power, and it becomes significantly worse when multiple parameters vary. As the resonance of the lattice compensation network is more complex than the traditional topologies, it is important to study its sensitivity performance. An accurate model of the circuit should be established to analyze the system sensitivity. It should be highlighted that each scenario only takes into account the impacts of one parameter variation on the output power and voltage. A MATLAB code is developed to generate a single parameter variation for each component in a lattice network. Results will be able to clearly demonstrate how changes in the design parameters and load will affect overall performance.

3.1. Sensitivity to Switching Frequency

A time-domain simulation is used to verify the operation lattice-series WPT system. Output voltage and power curves are measured under different operating frequencies. Figure 8 illustrates that the output voltage and output power reach their maximum values at the operating frequency of f = 85 kHz.

(a)

(b)
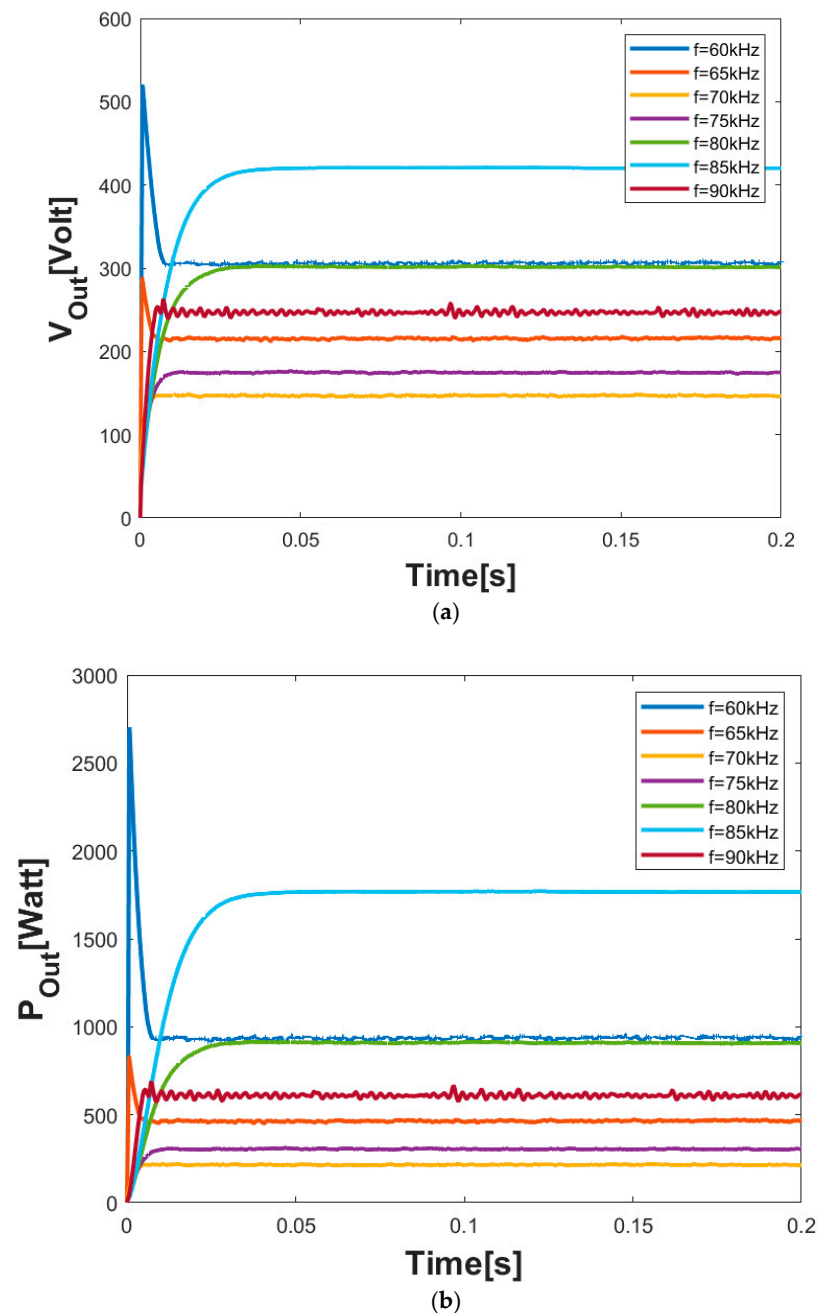
Figure 8. (**a**) Output voltages for different switching frequencies f = [60, 65, 70, 75, 80, 85, 90] kHz for the WPT system with a double-sided lattice compensation network at $V_{dc} = 300$ V; (**b**) Output powers for different switching frequencies f = [60, 65, 70, 75, 80, 85, 90] kHz for the WPT system with a double-sided lattice compensation network at $V_{dc} = 300$ V.

3.2. Sensitivity to Capacitor Size

As mentioned earlier, component values are key design parameters that adjust the system's maximum rated power. For this analysis, some codes are written in MATLAB R2022b/M-file, and characteristic curves are shown to execute the parallel parameter sweeps. The parameter sweeps assist in producing as many combinations as possible. The results from developed codes could be helpful for the designer to appropriately select the optimal sizes of each component. Note that other practical constraints like the voltage and current limitation of the components should be considered in a practical problem. The output from the program for five different values of capacitors is shown in Figure 9. It

shows that the optimal point for the capacitor is $C_z = 70$ µF; although, with $C_z = 60$ µF, the system output power can be achieved around 3000 watts, but output volage is near 700 volts, and it goes beyond what is typically found in an EV battery pack.

(a)

(b)
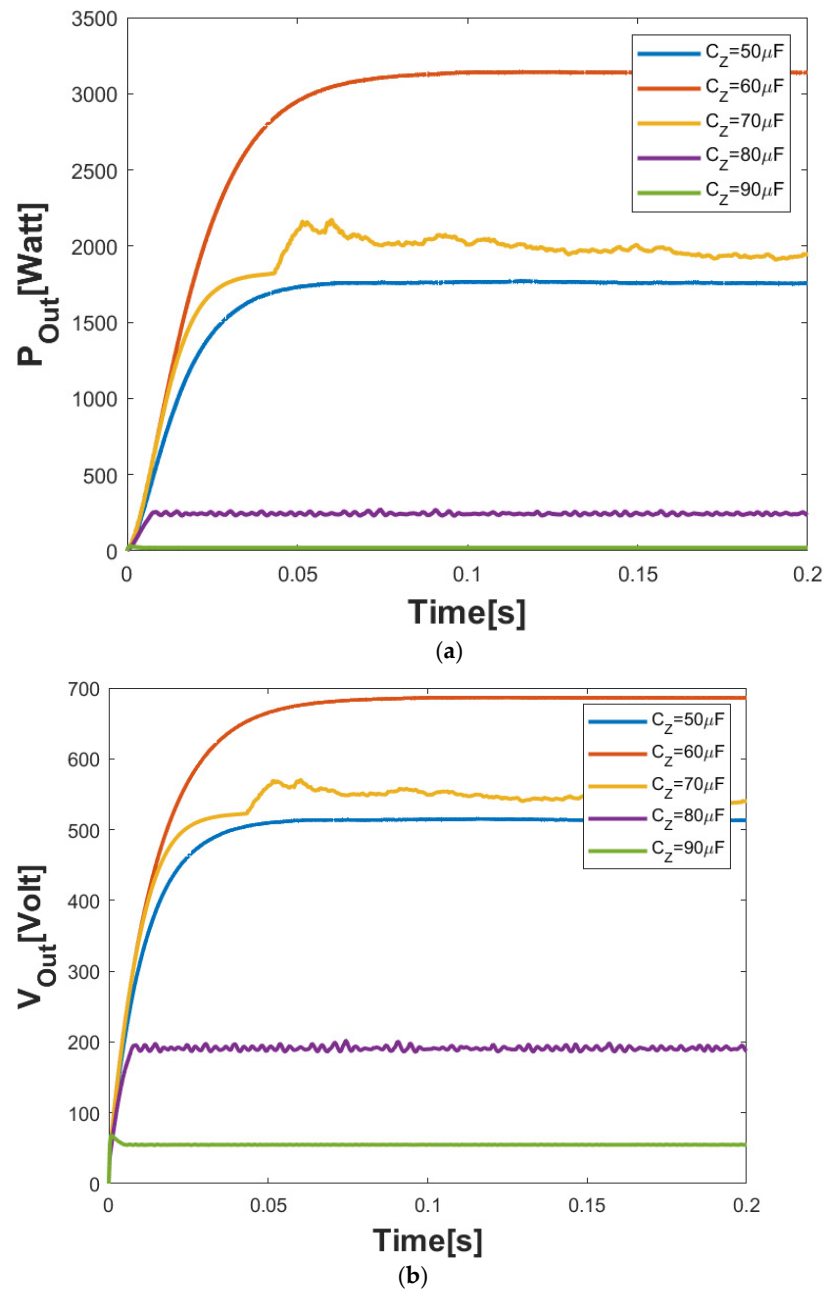
Figure 9. (**a**) Output voltages for different capacitors $C_z = [60, 65, 70, 75, 80, 85, 90]$ µF for the WPT system with a double-sided lattice compensation network at $V_{dc} = 300$ V; (**b**) Output powers for different capacitors $C_z = [60, 65, 70, 75, 80, 85, 90]$ µF for the WPT system with a double-sided lattice compensation network at $V_{dc} = 300$ V.

3.3. Sensitivity to Resistance Value

Finding the optimal load resistance is critical in designing a WPT system as it relates to the control strategy designed for the system. This is especially important when designing networks for low mutual inductance and high load resistance applications. The range of load resistance R_l in the simulation model is between 50 Ω and 150 Ω. Figures 10 and 11 show the primary and secondary sides.
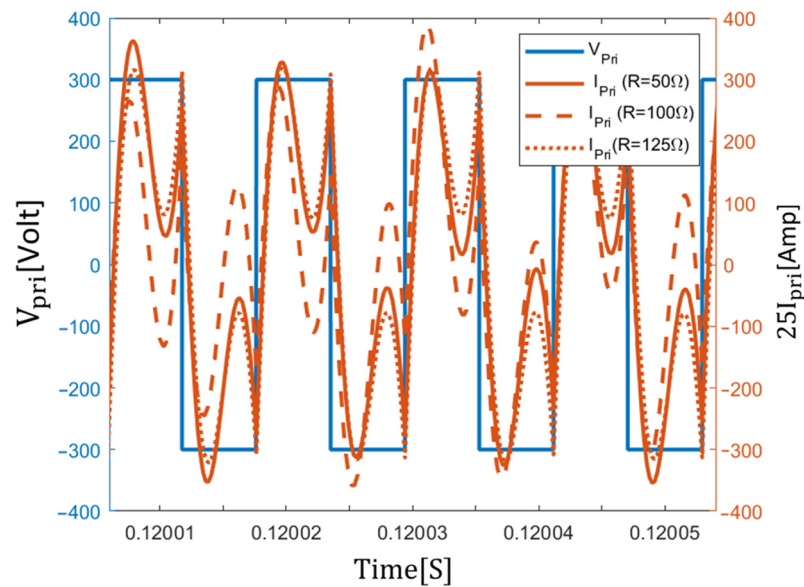
Figure 10. Primary side compensation network voltages and currents for varying loads for WPT system with double-sided lattice compensation network at $V_{dc} = 300$ V.
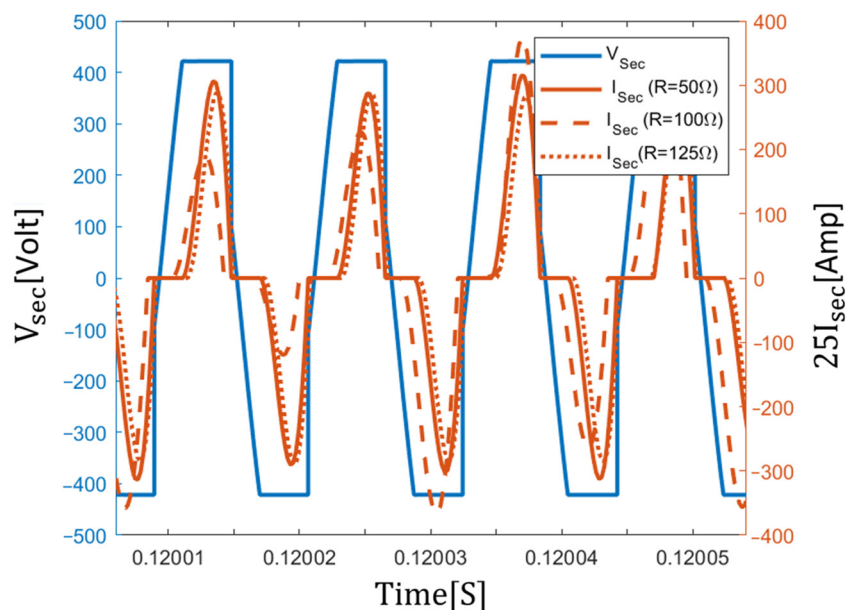
Figure 11. Secondary side compensation network voltages and currents for varying loads for WPT system with double-sided lattice compensation network at $V_{dc} = 300$ V.

Finding the optimal load, Figure 12 shows output power and efficiency against load resistance of the WPT system under different values of resistance at $V_{dc} = 300$ V. The primary side of the compensation network operates within a voltage range of approximately 430 volts, which is considered moderate and not excessively high. Drawing conclusions from the simulation results, it appears that the system demonstrates its peak efficiency and output power when the resistance is approximately 125 Ω. This is the optimal value during the charging. As can be seen in Figure 12, regardless of the target rated power, DC to DC efficiency can reach up to ~82%. The results of the sensitivity analysis indicate that fine-tuning certain parameters in the WPT system, such as the switching frequency, capacitor size, and load resistance, can effectively address sensitivity issues and maintain output power close to the nominal value. These adjustments are particularly impactful in enhancing system performance. Optimizing these parameters within specified ranges or

values can achieve better control over key performance metrics such as efficiency, power transfer capability, and voltage regulation. This approach allows you to design and optimize your WPT system to meet specific performance goals and address sensitivity challenges effectively. The results of the sensitivity analysis indicate that fine-tuning certain parameters in the WPT system, such as the switching frequency, capacitor size, and load resistance, can effectively address sensitivity issues and maintain output power close to the nominal value. These adjustments are particularly impactful in enhancing system performance. Optimizing these parameters within the specified ranges or values can achieve better control over key performance metrics such as efficiency, power transfer capability, and voltage regulation. This approach allows you to design and optimize your WPT system to meet specific performance goals and address sensitivity challenges effectively.
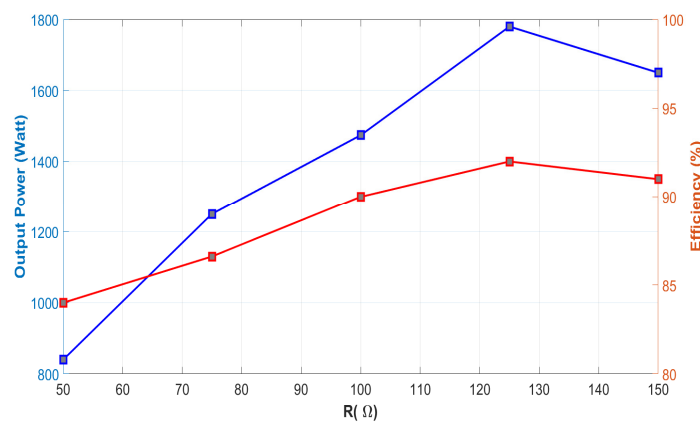
Figure 12. Output power and efficiency vs. load resistance for the WPT system with double-sided lattice compensation network at $V_{dc} = 300$ V.

4. Optimization

The optimization of the matching networks is a highly complex task because there are a large number of available designs. Intelligent algorithms are popular and useful to deal with system optimization problems. The genetic algorithm has many local optimal solutions, and the performance of the solution depends on the selection of an initial guess. In this article, a mixed integer linear programming algorithm (MILPA) is used to search for the optimal parameters to achieve the best overall system performance. It is an optimization solver capable of solving non-convex and mixed-integer programming [26]. In addition, it can also find the global optimal point for the optimization. Figure 13 shows the proposed procedure to design the resonant network components.
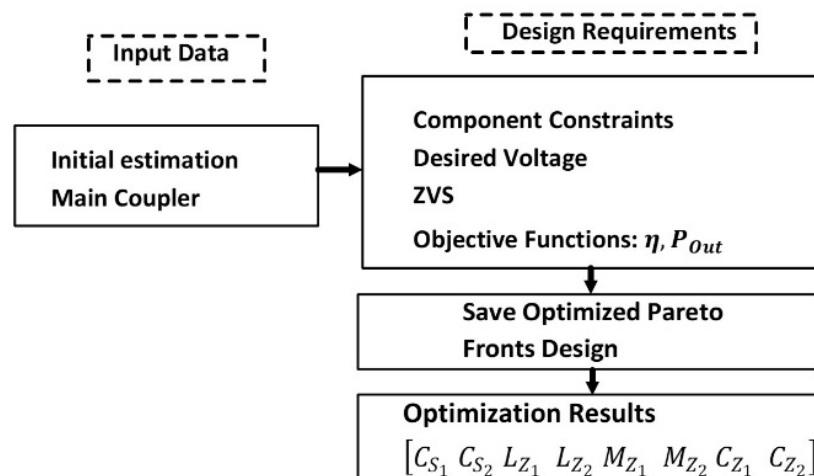
Figure 13. Procedure of the proposed optimized resonant network design.

In order to define the optimization problem comprehensively, it is crucial to specify different aspects of the problem. The initial step in the process is to identify the predefined values, as specified in Table 1, and subsequently establish the initial solution. Secondly, constraints, such as upper and lower bounds on currents and voltages, are crucial in optimization problems to maintain the solution within feasible operational limits. Finally, the definition of an objective function is a fundamental aspect of optimization problems. The primary optimization objectives are achieving the maximum output power (P_{out}) and the highest possible efficiency (η). The output power and efficiency are typically mutually constrained in power systems.

$$P_{out}(x_1,\ x_2,\ ..,\ x_n) = P_{in} - P_{loss} \tag{32}$$

$$\eta(x_1,\ x_2,\ ..,\ x_n) = \frac{P_{out}}{P_{in}} \tag{33}$$

Table 1. Specifications of WPT system in the simulation study.

Parameter	Symbol	Value
DC power supply	V_{dc}	300 V
Resonant frequency	f	85 kHz
Airgap between pads	d	100 mm
Primary coil inductance	L_{pri}	230 μH
Secondary coil inductance	L_{sec}	230 μH
Mutual inductance between main coil	L_M	73 μH

In this paper, each solution is defined by a vector, x, where $=[C_{s_1}, C_{s_2}, L_{z_1}, L_{z_2}, M_{z_1}, M_{z_2}, C_{z_1}, C_{z_2}]$.

In earlier works, a high-efficiency resonant converter was designed for a specific operating point. In this paper, the goal is to achieve a high-performance design for a wide range of load variations The objective function for a Li-ion battery is defined by the time-weighted average efficiency (TWAE) index, which is used to determine the optimal solution for efficiency under various conditions. [27]. The charging process for Li-ion batteries involves four essential stages. It begins with trickle charging to revive deeply depleted cells, followed by CC charging for a faster recharge, transitioning to CV charging to avoid overcharging, and finally, charge termination to ensure safety and full capacity typical charging. The profile for the Li-ion battery packs is depicted in Figure 14, illustrating the two primary charging modes: At the beginning of the charging process, the battery terminal voltage and current are at low levels, as indicated by point P_2. The CC charging mode is maintained until the battery terminal voltage rises to a maximum level, as denoted by P_1. In this case, the CV charging mode is engaged to make sure that the battery terminal voltage does not go above the maximum permissible limits. P_4 is maximum cell voltage, P_3 is midpoint between P_1 and P_2.
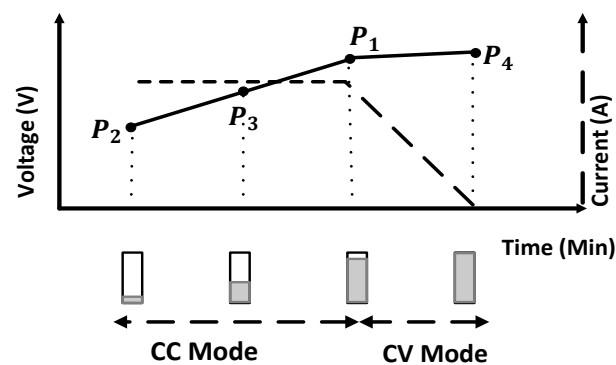
Figure 14. Typical charging profile of Li-ion battery.

$w = [w_1, w_2, w_3, w_4]$ is the weighting coefficients value for the system efficiencies in each sample operating points during charging process. This can be concluded as follows [27].

$$W = [\,0.03\;\; 0.767\;\; 0.126\;\; 0.074]$$ (34)

The objective function is defined as follows:

$$F = \mathrm{Max} \sum W \times \eta \times P_{out}$$ (35)

To simplify the analysis and reduce computation time, it is essential to make certain assumptions:

$$L_{z1} = L_{z2} = L_z$$ (36)

$$M_{z1} = M_{z2} = M_z$$ (37)

Due to a leakage in the winding-cross-coupled inductor M_z, it is less than L_Z, It complies with the following inequality:

$$0.10 L_z < M_z < 0.35 L_z$$ (38)

An iterative loop has been implemented to dynamically adjust the compensation parameters based on MILPA. A simulation script is developed for conducting a parameter sweep of variables (x). During each iteration of the MATLAB-based simulation, the values of output power (P_{out}) and efficiency (η) are extracted. In the presence of mutually conflicting objectives, the solution of problem (32) is not a unique optimal design, but a set of solutions and is commonly referred to as Pareto front because of the Pareto dominance concept. Figure 15 shows the result of an optimization with respect to efficiency and output. Each plotted data point corresponds to a different design variation, which indicates the maximum achievable power density for a specific efficiency. Critical boundary conditions are defined as P > 3000 watt and η > 0.85. The yellow region shows where both constraints are satisfied. It can be seen that the Pout has a maximum at a certain efficiency. For higher efficiencies, the Pout must be reduced. Optimal results are chosen from the Pareto-optimal fronts: x = [66 nF, 66 nF, 18 μH, 18 μH, 4.8 μH, 4.8 μH, 24 nF, 24 nF].
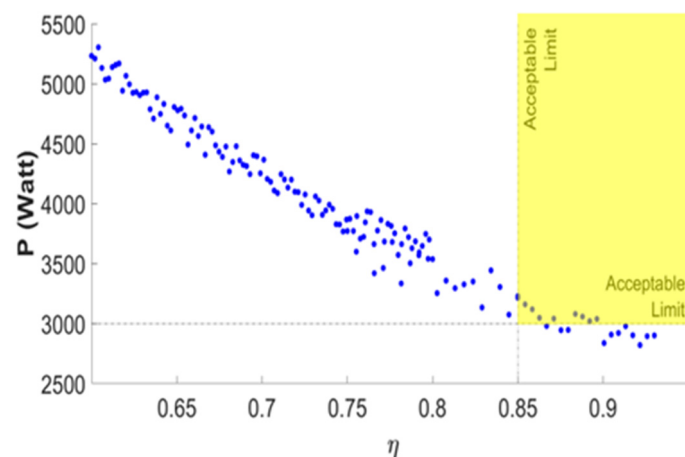
Figure 15. The projections of the obtained Pareto-optimal front for the WPT system with double-sided lattice compensation network at $V_{dc} = 300$ V.

5. Experimental Setup

According to the results of the analysis obtained from the simulation and in combination with the available resources in the lab, a scaled-down prototype of a WPT system with a double-sided lattice compensation network is designed and implemented. The parameters of the prototype are listed in Table 2.

Table 2. Specifications of the WPT system in the simulation study.

Parameter	Symbol	Value
DC power supply	V_{dc}	100 V
Resonant frequency	f	84.3 kHz
Airgap between pads	d	100 mm
Primary coil inductance	L_{pri}	228 µH
Secondary coil inductance	L_{sec}	228 µH
Mutual inductance between main coil	M	71 µH
Mutual inductance of lattice compensation	M_z	4.8 µH
Inductance of lattice compensation	L_z	18 µH
Primary series compensation capacitor	C_z	24 nF
Secondary series compensation capacitor	C_{s1}	66 nF
Radius and height winding-cross-coupled	C_{s2}	66 nF

Figure 16 illustrates the block diagram of the experimental setup, which is a WPT system implemented with double-sided lattice networks.. It comprises a DC power supply, a high-frequency inverter with SiC MOSFETs, two lattice resonant networks, a digital signal processor DSP, a gate driver board, a rectifier, and a resistor load bank. Four PWM signals are produced by a DSP and directed to a gate driver, which is employed for driving the gate of switches S1 to S4.
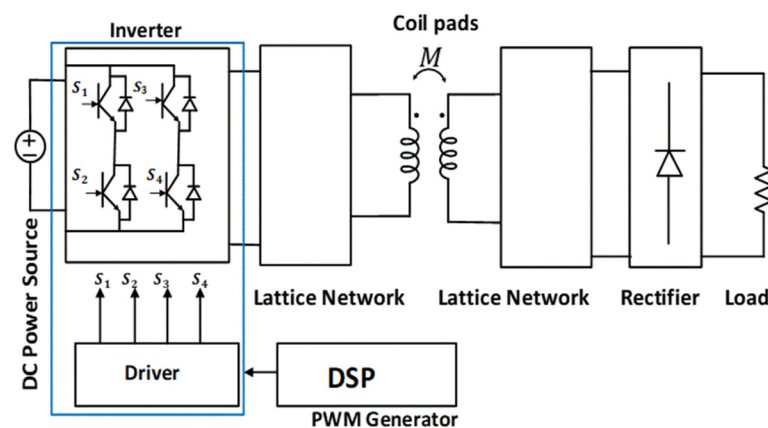
Figure 16. Experimental setup illustrated by a block diagram.

To verify the feasibility of the proposed WPT system, the WPT prototype is constructed as shown in Figure 17. The fabricated coil setup developed in the laboratory is shown in Figure 18. The magnetic pad is a circular made of 1500 strands of AWG 38 litz wire. The sizing and the number of turns of the magnetic couplers are based on a 3D finite element analysis model. The transmitter and receiver side coils are identical, with 28 turns on each side. The wire was placed on a coil former produced using 3D printing technology. Seven $240 \times 60 \times 5$ mm ferrite bars are placed in the back of the magnetic self-inductances, and mutual inductances of the couplers are measured by BK Precision. The total dimension of the magnetic coupler is 410×410 mm^2.

The FEA simulation results and the experimental measurement of the coupling factor are compared in Figure 19. It can be seen that the FEM simulation and experimental model matches closely. Winding-cross-coupled inductors are less expensive than magnetic-core inductors. This cost difference is because air-core inductors do not require magnetic cores, while magnetic-core can be relatively costly to manufacture. In this study, the winding-cross-coupled inductor has been constructed using litz wire, and its coil frame is composed of polyvinyl chloride (PVC), which exhibits a notable loss tangent, as indicated in Figure 18b. Manufacturing this structure is straightforward, and there is no need to introduce additional complexity. The top view of the coil former for a winding-cross-coupled inductor with 11 pie sections is shown in Figure 18c. The inductance of the coil

is determined by the coli former diameter and spacing of the wire. The compensating capacitors are created by connecting film capacitors together.
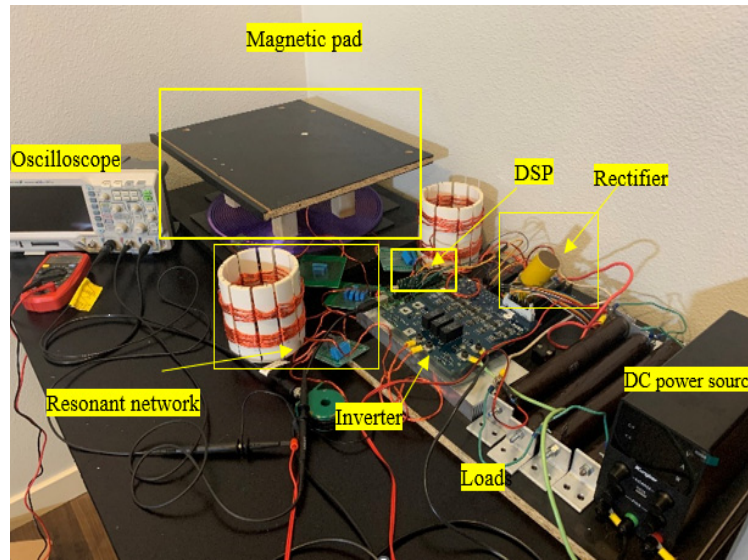
Figure 17. Experimental test setup used to validate the presented algorithm for the WPT system with a double-sided lattice compensation network at $V_{dc} = 100$ V.
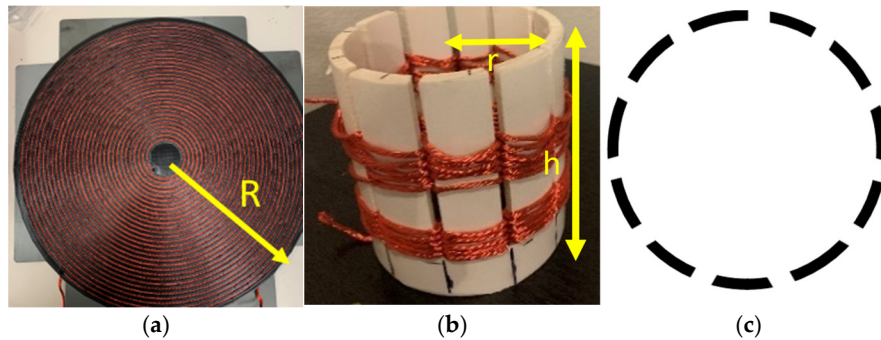
Figure 18. Prototype of a dual-coupled magnetic coupler. (**a**) Receiver magnetic coil pad in 3D printed coil former (R = 2.5″); (**b**) winding-cross-coupled inductor (h = 5″); (**c**) top view of a coil former for a winding-cross-coupled inductor with 11 sections.
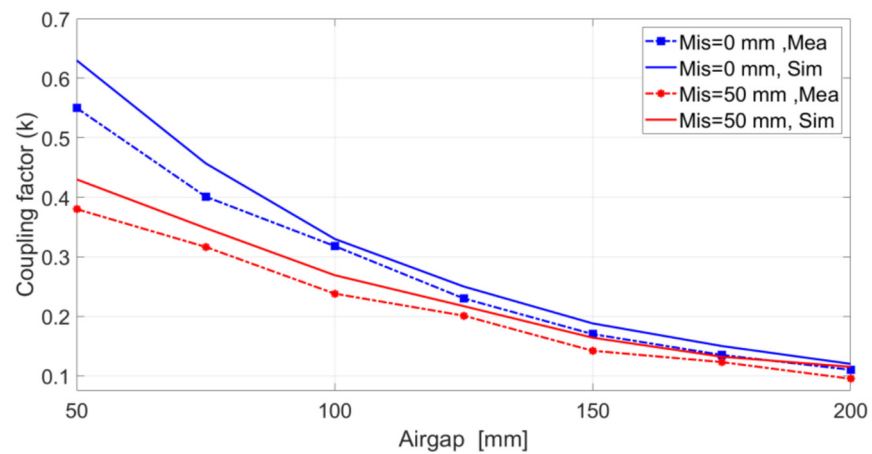
Figure 19. Comparison of the coupling factor at perfect alignment and 50 mm misalignment using FEM and measurements.

Based on the system, when the primary and secondary coils are well-aligned, the steady-state waveforms of the input voltage V_1 and input current I_1 as well as the output voltage V_2 and output current I_2, are shown in Figures 20 and 21, which confirm that the ZVS input is achieved.
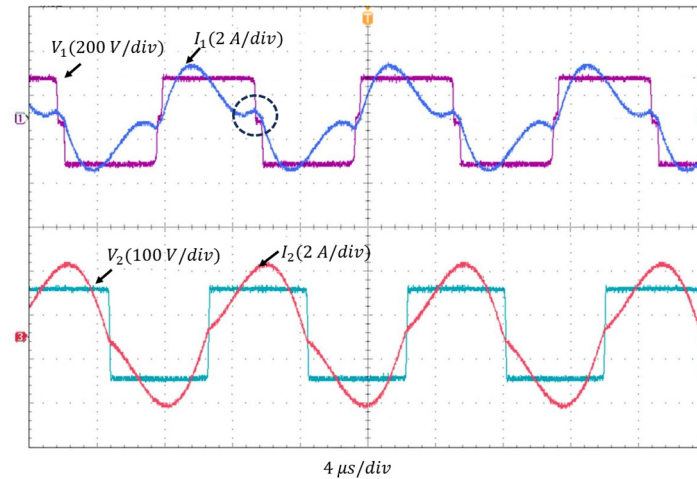
Figure 20. Experimental capture of the transient response at full load aligned case at $V_{DC} = 100$ V.
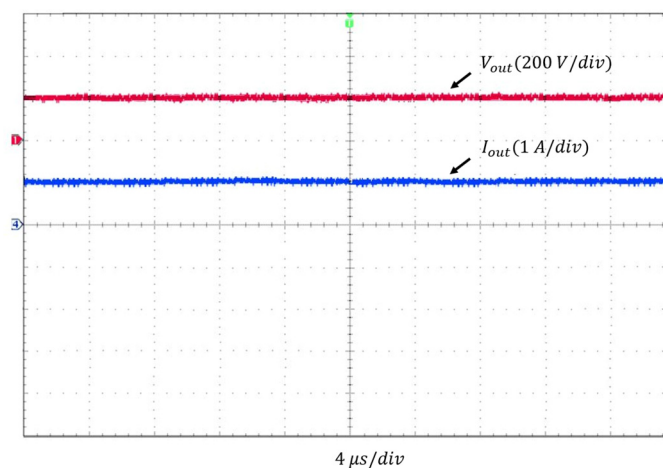
Figure 21. Experimental capture of output voltage and current the at full load aligned case at $V_{dc} = 100$ V.

Typically, in WPT systems with LLC-LLC compensation networks for an output voltage adjustment, an extra DC–DC converter is employed. The proposed system is capable of achieving soft switching during battery charging without requiring such converters. The combined inductance of each side ($2L_z$) is 36 µH. The discrepancy in compensation inductance is not significant when compared to the external inductance of the primary LCC circuit.

Table 3 outlines the key parameters of various compensator network structures. The majority of the existing designs aim at achieving power transfer for a single rated operating point, which makes them less suitable for variable output loads, such as batteries. This becomes especially problematic as the internal resistance of batteries tends to fluctuate during the charging period. The implementation of a single-phase shift angle control strategy in [28] the input inverter raises concerns about the WPT system's maximum efficiency. In [29], the authors explored a control strategy to dynamically manage the ZVS angle to maintain the rated output. The advantage of such control approaches lies in the implementation of CC/CV profiles with fewer components by eliminating DC–DC converters. However, this circuit configuration may induce larger losses for low-voltage

and high-current scenarios. References [30–32] discuss control strategies to maintain the rated output power by varying the input voltage and frequency of operation. However, many of the mentioned control strategies do not guarantee ZVS. In [14], the output voltage is regulated by a boost converter on the transmitter side. In [33], a supplementary DC–DC converter is inserted between the DC power supply and the inverter to regulate the output by adjusting the duty cycle of the high-frequency switching. However, practical feasibility is hampered due to the added power loss and increased cost associated with the DC–DC converter. Although the system proposed in this paper includes a higher count of passive elements, it exhibits performance comparable to other compensation networks discussed in recent literature, as depicted in Table 3. There is potential for efficiency improvement by enhancing the winding-cross-coupled inductor. Additionally, a larger input voltage in this system contributes to higher overall efficiency, as the driving circuit maintains constant loss.

Table 3. Comparison analysis of the proposed WPT system with previous work.

Refs	Compensation	P	Eff	Regulation	Extra Converter
[28]	LCC-S	77 W	84.1%	No	No
[29]	SS	10 W	86.2%	No	No
[30]	PP	10.8 W	74.7%	No	No
[31]	LLC-LLC	150 W	70%	No	No
[32]	LLC-S	64.8 W	77.5%	No	No
[14]	LLC-S	20 W	89%	Yes	Yes
[33]	S-LLC	1.2 KW	90.3%	Yes	Yes
This work	Lattice	200 W	86.3%	Yes	No

6. Conclusions and Future Work

In this article, a dual-coupled lattice WPT system is proposed to improve performance by achieving ZVS. The circuit's working principle of the lattice-based WPT system is presented in detail. A two-port network-based modeling approach for dual-coupled lattice WPT systems has been introduced. Following that, a MILP algorithm was implemented to optimize the WPT system's performance by tuning the compensation networks, which helps designers determine the value of winding-cross-coupled networks. This method changes the proposed system by eliminating the need for an auxiliary DC–DC converter, ensuring efficient charging across various load conditions. Finally, based on the proposed method, a scaled-down 200 W prototype was built to verify the feasibility and performance of the topology. Experimental results showed that the proposed WPT system could achieve a DC–DC efficiency higher than 86.3% at well-aligned power at a 100 mm air gap. The experimental results for the lattice-type WPT circuit showed good compliance with analytical and circuit simulations. Future research will perform a complete FEM analysis of the winding-cross-coupled inductors and integrate these inductors with the main coil to increase power density and improve system performance.

Author Contributions: Conceptualization, E.N.E. and I.B.; methodology E.N.E. and I.B. All authors have read and agreed to the published version of the manuscript.

References

1. Laha, A.; Kalathy, A.; Pahlevani, M.; Jain, P. A comprehensive review on wireless power transfer systems for charging portable electronics. *Eng* **2023**, *4*, 1023–1057. [CrossRef]
2. Patil, D.; McDonough, M.K.; Miller, J.M.; Fahimi, B.; Balsara, P.T. Wireless Power Transfer for Vehicular Applications: Overview and Challenges. *IEEE Trans. Transp. Electrif.* **2018**, *4*, 3–37. [CrossRef]
3. He, H.; Sun, F.; Wang, Z.; Lin, C.; Zhang, C.; Xiong, R.; Deng, J.; Zhu, X.; Xie, P.; Zhang, S.; et al. China's battery electric vehicles lead the world: Achievements in technology system architecture and technological breakthroughs. *Green Energy Intell. Transp.* **2022**, *1*, 100020. [CrossRef]
4. Ojha, T.; Raptis, T.P.; Passarella, A.; Conti, M. Wireless power transfer with unmanned aerial vehicles: State of the art and open challenges. *Pervasive Mob. Comput.* **2023**, *93*, 101820. [CrossRef]
5. Rong, C.; Duan, X.; Chen, M.; Wang, Q.; Yan, L.; Wang, H.; Xia, C.; He, X.; Zeng, Y.; Liao, Z. Critical Review of Recent Development of Wireless Power Transfer Technology for Unmanned Aerial Vehicles. *IEEE Access* **2023**, *11*, 132982–133003. [CrossRef]
6. Rayan, B.A.; Subramaniam, U.; Balamurugan, S. Wireless power transfer in electric vehicles: A review on compensation topologies, coil structures, and safety aspects. *Energies* **2023**, *16*, 3084. [CrossRef]
7. Sagar, A.; Kashyap, A.; Nasab, M.A.; Padmanaban, S.; Bertoluzzo, M.; Kumar, A.; Blaabjerg, F. A Comprehensive Review of the Recent Development of Wireless Power Transfer Technologies for Electric Vehicle Charging Systems. *IEEE Access* **2023**, *11*, 83703–83751. [CrossRef]
8. Sampath, J.; Khan, A. Design, challenges, and trends of inductive power transfer couplers for electric vehicles: A review. *IEEE J. Emerg. Sel. Top. Power Electron.* **2020**, *9*, 6196–6218.
9. Luo, Z.; Wei, X.; Pearce, M.G.S.; Covic, G.A. Multiobjective Optimization of Inductive Power Transfer Double-D Pads for Electric Vehicles. *IEEE Trans. Power Electron.* **2021**, *36*, 5135–5146. [CrossRef]
10. Namadmalan, A.; Tavakoli, R.; Goetz, S.M.; Pantic, Z. Self-Aligning Capability of IPT Pads for High-Power Wireless EV Charging Stations. *IEEE Trans. Ind. Appl.* **2022**, *58*, 5593–5601. [CrossRef]
11. Maciej, S.J. Analysis of the Wireless Power Transfer System Using a Finite Grid of Planar Circular Coils. *Energies* **2023**, *16*, 7651. [CrossRef]
12. Rahulkumar, J.; Narayanamoorthi, R.; Vishnuram, P.; Balaji, C.; Gono, T.; Dockal, T.; Gono, R.; Krejci, P. A review on resonant inductive coupling pad design for wireless electric vehicle charging application. *Energy Rep.* **2023**, *10*, 2047–2079.
13. Zhang, Y.; Pan, W.; Wang, H.; Shen, Z.; Wu, Y.; Dong, J.; Mao, X. Misalignment-tolerant dual-transmitter electric vehicle wireless charging system with reconfigurable topologies. *IEEE Trans. Power Electron.* **2022**, *37*, 8816–8819. [CrossRef]
14. Dayerizadeh, A.; Lukic, S. Saturable inductors for superior reflexive field containment in inductive power transfer systems. In Proceedings of the IEEE Applied Power Electronics Conference and Exposition (APEC), San Antonio, TX, USA, 4–8 March 2018; pp. 3183–3188. [CrossRef]
15. Chen, Y.; Yang, B.; Kou, Z.; He, Z.; Cao, G.; Mai, R. Hybrid and Reconfigurable IPT Systems With High-Misalignment Tolerance for Constant-Current and Constant-Voltage Battery Charging. *IEEE Trans. Power Electron.* **2018**, *33*, 8259–8269. [CrossRef]
16. Ramezani, A.; Narimani, M. Optimal Design of Fully Integrated Magnetic Structure for Wireless Charging of Electric Vehicles. *IEEE Trans. Transp. Electrif.* **2021**, *7*, 2114–2127. [CrossRef]
17. Zhu, H.; Zhang, B.; Wu, L. Output power stabilization for wireless power transfer system employing primary-side-only control. *IEEE Access* **2020**, *8*, 63735–63747. [CrossRef]
18. Ma, C.; Qu, X.; Liu, J.; Tan, L. A Novel Cascaded Buck Active Rectifier With Arbitrary Impedance Conversion Ratio for Inductive Power Transfer System. *IEEE Trans. Transp. Electrif.* **2024**, *1*. [CrossRef]
19. Babaki, A.; Vaez-Zadeh, S.; Zakerian, A.; Covic, G.A. Variable-frequency retuned WPT system for power transfer and efficiency improvement in dynamic EV charging with fixed voltage characteristic. *IEEE Trans. Energy Convers.* **2021**, *36*, 2141–2151. [CrossRef]
20. Feng, H.; Dayerizadeh, A.; Lukic, S.M. A Coupling-Insensitive X-Type IPT System for High Position Tolerance. *IEEE Trans. Ind. Electron.* **2021**, *68*, 6917–6926. [CrossRef]
21. Corti, F.; Intravaia, M.; Reatti, A.; Grasso, F.; Grasso, E.; Cabrera, A.T. Component design procedure for LCC-S wireless power transfer systems based on genetic algorithms and sensitivity analysis. *IET Power Electron.* **2024**, *17*, 906–918. [CrossRef]
22. Huang, L.; Hu, A.P.; Swain, A.K.; Su, Y. Z-Impedance Compensation for Wireless Power Transfer Based on Electric Field. *IEEE Trans. Power Electron.* **2016**, *31*, 7556–7563. [CrossRef]
23. Oleksandr, H.; Roncero-Clemente, C. Resonant and Z-source multilevel inverters. In *Multilevel Inverters*; Academic Press: Cambridge, MA, USA, 2021; pp. 217–257.
24. Chua, L.O.; Desoer, C.A.; Kuh, E.S. *Linear and Nonlinear Circuits*; McGraw Hill: New York, NY, USA, 1987.
25. Alrubaie, A.J.; Salem, M.; Yahya, K.; Mohamed, M.; Kamarol, M. A comprehensive review of electric vehicle charging stations with solar photovoltaic system considering market, technical requirements, network implications, and future challenges. *Sustainability* **2023**, *15*, 8122. [CrossRef]
26. Samuel, B.; Letchford, A.N. Non-convex mixed-integer nonlinear programming: A survey. *Surv. Oper. Res. Manag. Sci.* **2012**, *17*, 97–106.
27. Fang, Z.; Cai, T.; Duan, S.; Chen, C. Optimal Design Methodology for LLC Resonant Converter in Battery Charging Applications Based on Time-Weighted Average Efficiency. *IEEE Trans. Power Electron.* **2015**, *30*, 5469–5483. [CrossRef]

28. Li, Z.; Wei, G.; Dong, S.; Song, K.; Zhu, C. Constant current/voltage charging for the inductor–capacitor–inductor-series compensated wireless power transfer systems using primary-side electrical information. *IET Power Electron.* **2018**, *11*, 2302–2310. [CrossRef]

29. Kavimandan, U.D.; Mahajan, S.M.; Van Neste, C.W. Analysis and Demonstration of a Dynamic ZVS Angle Control Using a Tuning Capacitor in a Wireless Power Transfer System. *IEEE J. Emerg. Sel. Top. Power Electron.* **2021**, *9*, 1876–1890. [CrossRef]

30. Tian, J.; Hu, A.P. A DC-Voltage-Controlled Variable Capacitor for Stabilizing the ZVS Frequency of a Resonant Converter for Wireless Power Transfer. *IEEE Trans. Power Electron.* **2017**, *32*, 2312–2318. [CrossRef]

31. Lu, F.; Zhang, H.; Hofmann, H.; Mi, C.C. A Double-Sided LC-Compensation Circuit for Loosely Coupled Capacitive Power Transfer. *IEEE Trans. Power Electron.* **2018**, *33*, 1633–1643. [CrossRef]

32. Kim, D.-H.; Ahn, D. Self-Tuning LCC Inverter Using PWM-Controlled Switched Capacitor for Inductive Wireless Power Transfer. *IEEE Trans. Ind. Electron.* **2019**, *66*, 3983–3992. [CrossRef]

33. Bozorgi, A.M.; Tavakoli, R.; Farasat, M. Unified Coil and Compensation Network Design for Improving Wireless Power Transfer Efficiency Over Wide Output Load Variation Ranges. *IEEE J. Emerg. Sel. Top. Power Electron.* **2022**, *10*, 2190–2200. [CrossRef]